ACS Catalysis

pubs.acs.org/acscatalysis Research Article

Defect-Induced Synergetic Effect of Bi-Based Compounds for One-Pot Conversion of Organic Pollutants into CO via Coupling Photodegradation of Carbamazepine with Photoreduction of CO_2

Ling-Ling Zheng, Lei Tian, Long-Shuai Zhang, Jian Yu, Ying Chen, Qian Fu, Xiao-Zhen Liu, Dai-She Wu, and Jian-Ping Zou*

Cite This: *ACS Catal.* 2024, 14, 2134−2143 Read Online

ACCESS | Metrics & More | Article Recommendations | Supporting Information

ABSTRACT: The waste of carbon sources and greenhouse gas production during wastewater treatment have become extremely important environmental issues. Herein, the $BiOBr/BiVO_4$ compounds with defect-induced frustrated Lewis acid−base pairs (DFLPs) and internal charge transfer were fabricated to convert the organic pollutants into CO with nearly 100% selectivity. The oxygen vacancy (O_v) induced the built-in electric field in $BiOBr/BiVO_4$ to create directional charge transfer from BiOBr to $BiVO_4$. Density functional theory (DFT) calculations prove that the O_v combines its adjacent hydroxyls to form the DFLP active sites that can additionally capture and activate CO_2. Meanwhile, the active sites in $BiOBr/BiVO_4$ reduce the formation-free energy of the COOH* intermediates, which is the key rate-limiting step to convert CO_2 to CO with high selectivity. This system has achieved selective conversion of value-added chemicals from organic pollutant degradation and provides a theoretical basis for actual wastewater recycling of carbon sources.

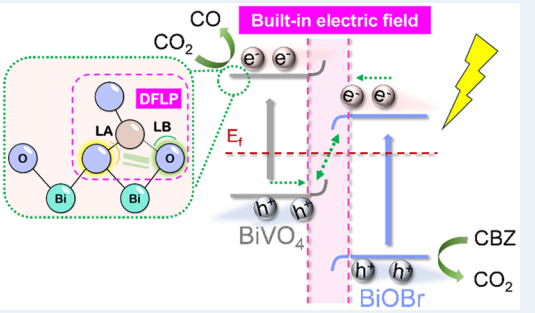

KEYWORDS: *carbon source recovery, charge transfer, frustrated Lewis pairs, oxygen vacancy, photocatalysis*

1. INTRODUCTION

In industry, technologies have been proposed for the harmless treatment of organic wastewater with CO_2 as the final product that was directly released into the atmosphere.[1−3] However, secondary waste gas pollution,[4] high thermodynamic stability (C═O, 750 kJ mol^{-1})[5] of CO_2, and carbon source shortages[6] during sewage treatment have restricted the processing and violated the carbon-neutral economy.[7] Therefore, converting the generated flue gas from pollutant removal into value-added chemicals is a promising route to mitigate the carbon source waste and greenhouse effect.

Recently, numerous reports have explored the sustainable conversion of pollutants through photocatalytic,[8] electrocatalytic,[9] or other coupling technologies.[10] However, the inevitable significant consumption of electrical energy during electrochemical processes or the necessary addition of the extra oxidant to trigger the reaction has limited the wide application of these systems, and the mechanism of the sustainable conversion of pollutants is still unclear. Additionally, the low selectivity of products[11] and uncontrolled emission of CO_2 from synchronous reactions undoubtedly[12] increased the disposal cost of the subsequent solid−liquid or gas separation. Among all the treatments, artificial photosynthesis, which relies on inexhaustible and sustainable solar energy, is regarded as a dream reaction to meet the carbon source recovery from pollutant degradation.[13,14] Generally, the high charge recombination and randomly distributed oxidation/reduction catalytic sites strongly confine the efficiency and selectivity of organic pollutant conversion.[15] Hence, it is urgent to design an ideal catalyst with directed charge transmission and undisturbed oxidation−reduction active sites for the sustainable conversion of pollutants.

Based on the previous literature, simultaneously decorating reductive and oxidative cocatalysts on the core−shell structures[16] or crystalline semiconductors with delicately engineered facets[17] was an ideal way to spatially separate the catalytic sites. However, the distribution of dual cocatalysts on the surface of the catalyst in an ordered manner is challenging and requires complicated structural design and synthetic methodologies. Surprisingly, composite catalysts with specified regulation provide a versatile platform to realize the desired frameworks with spatially separated redox centers. Among kinds of photocatalysts, bismuth-based materials have been

Received: October 9, 2023
Revised: December 26, 2023
Accepted: December 27, 2023

https://doi.org/10.1021/acscatal.3c04820
ACS Catal. 2024, 14, 2134−2143

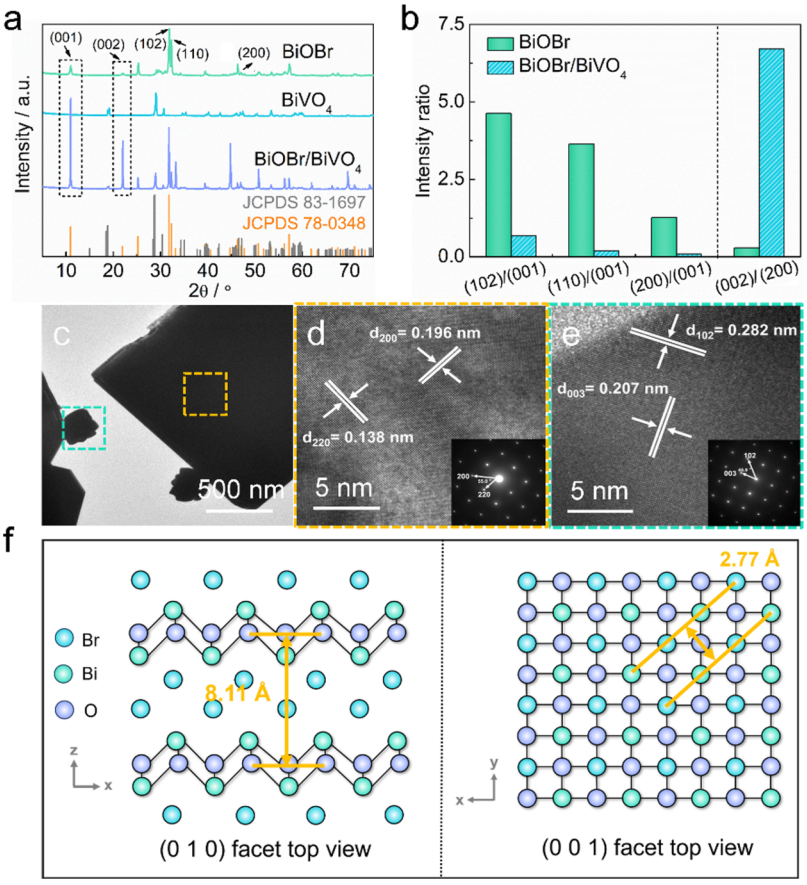

Figure 1. (a) XRD patterns of the catalysts. (b) The corresponding ratios of peak intensity for BiOBr and $BiOBr/BiVO_4$. (c) TEM and (d, e) HRTEM and SAED pattern of $BiOBr/BiVO_4$. (f) Atomic structure of (0 1 0) and (0 0 1) surfaces of BiOBr on top view.

known as efficient solar-driven photocatalysts for a variety of catalytic reactions that benefit from the regulated electronic structure and suitable band gap.[18] The heterojunction constructed by two bismuth-based catalysts has been confirmed as a promising redox system due to the efficient charge separation and photoinduced charges with high redox potentials.[19] Thus, it is desirable to develop bismuth-based hybrids with tailored active sites and noninfluencing oxidation/reduction reactions to achieve high efficiency and selectivity of carbon source recycling from organic pollutants.

Herein, $BiOBr/BiVO_4$ compounds with a defect-induced synergetic effect were developed via a one-pot ultrafast microwave hydrothermal method. The oxygen vacancy (O_v) concurrently induced the surface active sites and oriented charge transfer in $BiOBr/BiVO_4$ to efficiently mineralize the carbamazepine (CBZ, a typical antibiotic pollutant) and reduce the CO_2 with highly selective CO production. This system provides instructive guidelines for realizing carbon neutralization by low-carbon emissions in actual wastewater remediation.

2. EXPERIMENTAL SECTION

2.1. Materials. All of the chemicals during the synthesis were commercially available and used without further purification. Bismuth(III) nitrate pentahydrate ($Bi(NO_3)_3 \cdot 5H_2O$, AR), ammonium metavanadate (NH_4VO_3, AR), and potassium bromide (KBr, AR) were supplied from Aladdin Biochemical Technology Co., Ltd. (Shanghai, China). Methanol (CH_3OH, AR) and nitric acid (HNO_3, 68−70 wt %) were supplied from Xilong Chemical Co., Ltd. (Guangzhou, China).

2.2. Preparation of Photocatalysts. $BiOBr/BiVO_4$ compounds were prepared by a one-pot, ultrafast microwave hydrothermal method. In the synthetic system, $Bi(NO_3)_3 \cdot 5H_2O$ (6 mmol) was dissolved in nitric acid solution (15 mL, 1.0 M) under ultrasonic agitation, and then NH_4VO_3 (3 mmol) was added to obtain the $BiVO_4$ precursor. Briefly, a certain amount of KBr was added into the above precursor solution with vigorous stirring to obtain a yellowish solution. The obtained mixture solution was transferred to a borosilicate glass vessel with a capacity of 20 mL; after 1 min of stirring, the suspension was subjected to microwave hydrothermal treatment at 353 K for 30 min. Finally, the obtained precipitate was separated by centrifugation, washed three times with deionized water, and dried at 353 K. The obtained samples were named $BiOBr/BiVO_4$.

2.3. Characterizations. The crystallographic structure of the as-prepared samples was confirmed via X-ray diffraction (XRD) measurements (Bruker, Germany, with Cu Kα radiation). The morphology of the catalysts was recorded by scanning electron microscopy (SEM, J FEI, Hillsboro, OR, USA), transmission electron microscopy (TEM, JEOL model JEM 2010 EX instrument), high-resolution transmission electron microscopy (HRTEM), and selected-area electron diffraction (SAED). The X-ray photoelectron spectroscopy (XPS, VG 250 Escalab spectrometer) was measured to analyze the elemental composition and valence state of the samples. The Bi^{3+} ions leaching during the reaction were measured from

https://doi.org/10.1021/acscatal.3c04820
ACS Catal. 2024, 14, 2134−2143

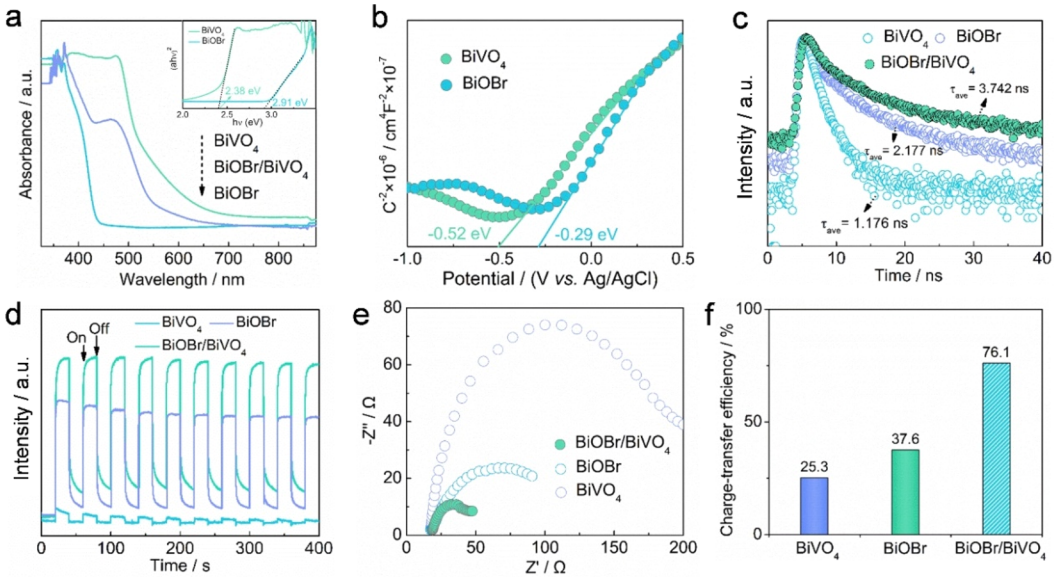

Figure 2. (a) UV−vis DRS spectra of $BiVO_4$, BiOBr, and $BiOBr/BiVO_4$ (inset is the plot of $(\alpha h\nu)^{1/2}$ vs photon energy ($h\nu$)). (b) Mott−Schottky plots of $BiVO_4$ and BiOBr. (c) TRPL spectra, (d) photocurrent density, (e) electrochemical impedance spectra, and (f) surface charge-transfer efficiency of $BiVO_4$, BiOBr, and $BiOBr/BiVO_4$.

the inductively coupled plasma-optical emission spectrometer (ICP-OES, PerkinElmer, Elmer Optima 2000DV). Ultraviolet−visible diffuse reflectance spectra (UV−vis DRS) were recorded with a UV−vis spectrophotometer (UV-2550, Shimadzu) with $BaSO_4$ as the reflectance standard. The efficiency of carrier separation was measured via the photoluminescence (PL, Hitachi F-4500) spectra and time-resolved fluorescence decay spectroscopy (TRPL, FS5 spectrofluorometer, Edinburgh Instruments, 380 nm picosecond pulsed diode laser as the excitation source). Electron paramagnetic resonance (EPR, Bruker EMX-10/12 spectrometer) was carried out to determine the vacancy in the samples and active species during the reaction. Electrochemical measurements were measured via a CHI 660D electrochemical workstation (Shanghai Chenhua, China) with a three-electrode cell system.

2.4. Catalytic Oxidation Reaction. The one-pot conversion of CBZ was carried out in a Pyrex top-irradiation reaction vessel connected to a gas-closed system (Ceaulight, Beijing, CEL-PAEM-D8CEL-PAEM-D). Detailed experiments were discussed in the Supporting Information. A 300 W Xe lamp (wavelength range: 350 nm $\leq \lambda \leq$ 780 nm; light intensity: 160 mW/cm^2) was used as the simulated sunlight. First, 30 mg of sample was added into the homemade reactor (250 mL volume with a quartz cover) with 100 mL of aqueous solution containing CBZ pollutants and NaOH (0.01 M). Then, the closed reactor was rinsed several times with an oil pump to completely exhaust the air. After that, the photocatalytic reaction was carried out under simulated sunlight irradiation for 4 h. The temperature of the reaction solution was maintained at 6 °C by an external flow of cold water (Ceaulight, Beijing, CEL-CR300CEL-CR300) during the reaction. Finally, the generated gaseous mixture was collected by a gas chromatograph (Ceaulight, Beijing, GC7920) equipped with a hydrogen flame ionization detector (FID). The concentration of pollutants was analyzed by high-performance liquid chromatography (HPLC, Thermo U3000) with a TC-C18 reverse-phase column (150 × 4.6 mm, 5 μm, Agilent).

2.5. Density Functional Theory (DFT) Calculations. The present first principle DFT calculations were supported by the Ceshigou Research Service, which was performed by the Vienna Ab initio Simulation Package (VASP) with the projector augmented wave (PAW) method. Detailed information about the calculation procedure is provided in the Supporting Information.

3. RESULTS AND DISCUSSION

3.1. Characterization of the Catalyst. The phase structures of $BiVO_4$, BiOBr, and $BiOBr/BiVO_4$ were determined via XRD analysis in Figure 1a. It exhibits that $BiVO_4$ and BiOBr coincide with the monoclinic scheelite bismuth vanadate (JCPDS 83-1697)[20] and tetragonal phase bismuth oxybromide (JCPDS 78-0348),[21,22] respectively. All the diffraction peaks of hybrids possess similar peak positions to those of $BiVO_4$ and BiOBr but different relative peak intensities. As shown in Figure 1b, the intensity ratios of (1 0 2), (1 1 0), and (2 0 0) to (0 0 1) in BiOBr are much higher than that of the $BiOBr/BiVO_4$ while the ratio of (0 0 2) to (2 0 0) was the opposite, indicating the change of dominated facets of the substrate from the (0 1 0) to the (0 0 1) facet with better hole-accumulating ability.[20] The TEM and SAED patterns were further measured to prove the orientation facets in catalysts.[23,24] Figure 1c reveals that the morphology of $BiOBr/BiVO_4$ was the nanosheets surrounded by nanoparticles. As shown in Figure 1d, the top facet of the square-shaped BiOBr side of the hybrid shows a lattice fringe with a spacing of 0.196 and 0.138 nm, corresponding to the (2 0 0) and (2 2 0) planes, respectively. The inset SAED pattern displays clear diffraction spots with diffraction planes, and the cross angle is 55.0°, which is identical with the theoretical value of the (0 0 1) facet in the tetragonal BiOBr. The lattice fringe and the distinct diffraction spots of the $BiVO_4$ side of the hybrids in Figure 1e indicate the exposed (0 0 4) planes.[25] The HRTEM and SAED pattern in Figure S2 reveals the clear lattice fringe with a cross angle of about 53.4° which was identical with the theoretical value in the standard of the

https://doi.org/10.1021/acscatal.3c04820
ACS Catal. 2024, 14, 2134−2143

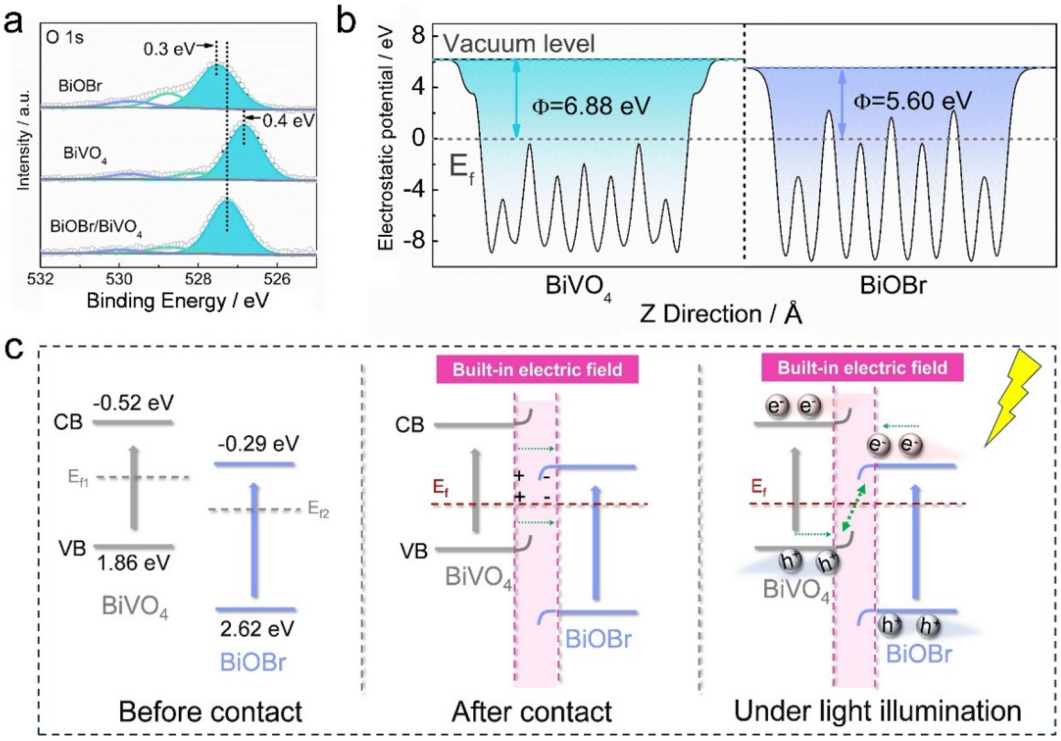

Figure 3. (a) High-resolution XPS pattern of the O 1s of $BiVO_4$, BiOBr, and $BiOBr/BiVO_4$. (b) Calculated work function of $BiVO_4$ and BiOBr. (c) Scheme of speculative interface charge transmission and electric field over $BiOBr/BiVO_4$ under different conditions: (left) before contact, (middle) after contact, and (right) under light illumination.

dominated (0 1 0) facets in circular BiOBr nanosheets, demonstrating the introduction of $BiVO_4$ altered the dominant plane of BiOBr from (0 1 0) to (0 0 1). Figure 1f reveals that the (0 1 0) facet of BiOBr possesses an open channel characteristic, while the (0 0 1) facet has a closed and regular structure, which was favored to confine the circulation of water and pollutants in the microenvironment. In theory, the oxidation and reduction reactions are preferable to occur on the (0 0 1) facets of BiOBr and (0 0 4) facets of $BiVO_4$, respectively.[21,26] These results suggested the one-pot synthesis changed the internal structure and dominant plane of $BiOBr/BiVO_4$ to separate the mineralization of pollutant and carbon source recovery.

The sunlight utilization and absorption edge of the $BiVO_4$, BiOBr, and $BiOBr/BiVO_4$ hybrids were evaluated based on UV−vis DRS. As shown in Figure 2a, the spectral response of the $BiOBr/BiVO_4$ hybrids with a light absorption edge extended to ∼582 nm, exhibiting excellent light absorption and utilization ability toward ultraviolet light and part of the visible region. The band structures of $BiVO_4$ and BiOBr were measured by the Tauc diagram and Mott−Schottky spectra. Based on the plots of $(\alpha h\nu)^{1/2}$ versus photon energy ($h\nu$), the band gap energies (E_g) of $BiVO_4$ and BiOBr were calculated to be 2.38 and 2.91 eV, respectively.[24] In addition, the positive slope of the Mott−Schottky plots for $BiVO_4$ and BiOBr in Figure 2b indicates their n-type characteristics, and their flat band potentials were measured to be −0.52 and −0.29 V (vs RHE), respectively, implying that $BiVO_4$ and BiOBr are appropriate for both proton reduction and water oxidation thermodynamically. We carried out the optical and electrochemical measurements to analyze the charge transfer and separation of the as-prepared samples. As shown in Figure S3, $BiOBr/BiVO_4$ exhibits weaker steady-state PL intensity than that of the other catalysts, which indicates its inhibitive recombination of the photogenic electron−hole pair. The TRPL spectra in Figure 2c and Table S1 revealed the lifetimes of the photogenerated charges of catalysts. The mean fluorescence lifetime of $BiOBr/BiVO_4$ (τ_{ave} = 3.742 ns) was significantly longer than those of $BiVO_4$ (τ_{ave} = 1.176 ns) and BiOBr (τ_{ave} = 2.177 ns). The slower quenching and decay of $BiOBr/BiVO_4$ imply the high extent of radiative relaxation pathways, which may be attributed to the internal structure of $BiOBr/BiVO_4$ that drives the photocatalytic reaction via the efficient exciton dissociation to produce photogenerated charges. Electrochemical analyses in Figures 2d,e and S4 reveal a higher photocurrent response and faster transfer of photogenerated electrons over $BiOBr/BiVO_4$ than the other catalysts, indicating a lower resistance and faster transfer of photogenerated electrons of the hybrids. The improved surface charge-transfer efficiency (η_{trans}) of $BiOBr/BiVO_4$ (ca. 76.1%) estimated by measuring the photocurrent density under linear sweep voltammetry (LSV) is shown in Figures 2f and S5, demonstrating the acceleration charge transfer between $BiVO_4$ and BiOBr. Therefore, the distinctly superior optical and electrochemical properties of $BiOBr/BiVO_4$ revealed the internal structure can accelerate the charge transfer between $BiVO_4$ and BiOBr.

As shown in Figure 3a, the high-resolution XPS pattern of O 1s revealed the signals belonging to the Bi−O bond in $BiOBr/BiVO_4$ were shifted to higher binding energy compared with those in BiOBr while showing an opposite trend with $BiVO_4$, indicating a lower electron density around $BiVO_4$ in hybrids.[27,28] Therefore, it can be speculated that there existed a strong electron interaction that induced the electron transfer from BiOBr to $BiVO_4$. DFT calculations were performed to determine the work function of the catalysts to probe the flow

https://doi.org/10.1021/acscatal.3c04820
ACS Catal. 2024, 14, 2134−2143

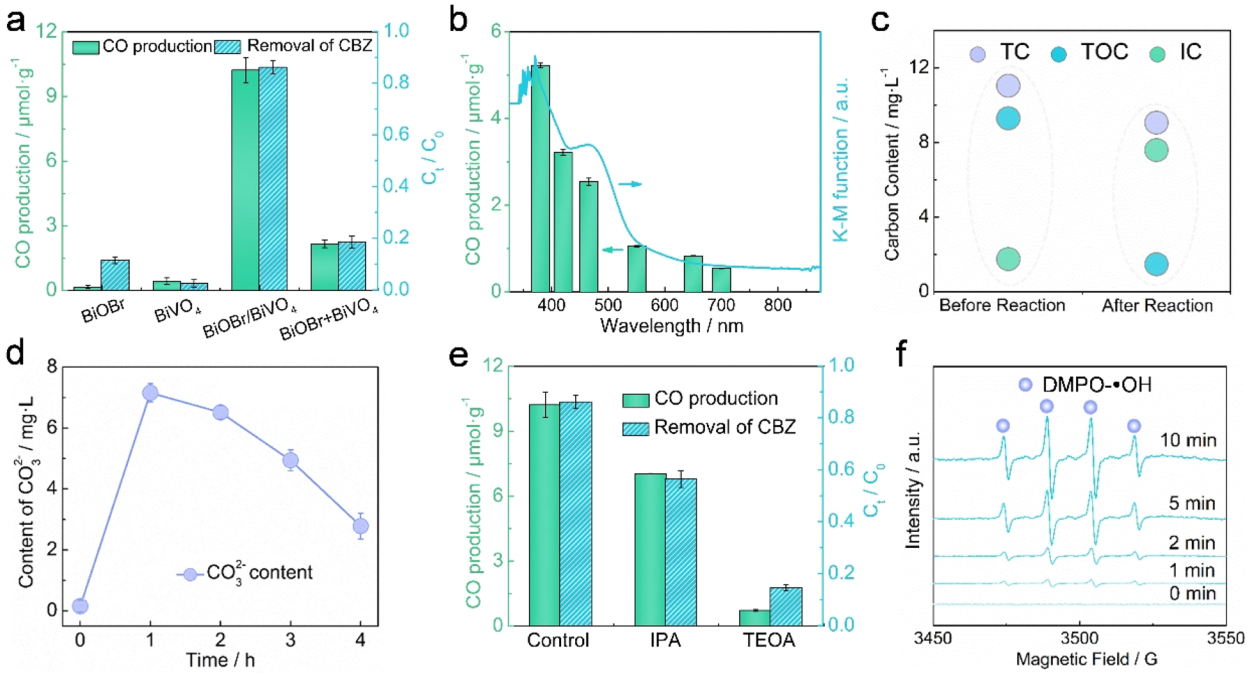

Figure 4. (a) Photocatalytic pollutant conversion performance of $BiVO_4$, BiOBr, $BiOBr/BiVO_4$, and $BiVO_4$+BiOBr. (b) The wavelength dependence of CO production, (c) TC, TOC, and IC content before and after reaction, (d) variation of CO_3^{2-} with the irradiation time, (e) conversion efficiency after adding different scavengers, and (f) EPR spectra of DMPO-·OH over $BiOBr/BiVO_4$.

and charge transfer between the interfaces.[29,30] As shown in Figure 3b, the calculation results exhibit $BiVO_4$ with high-level work function (6.88 eV) while BiOBr results in a lower work function of 5.60 eV. Combined with the test of the band gap, the initial state of the band structure diagram of $BiVO_4$ and BiOBr before contact is shown in Figure 3c, left. Due to the difference of the Fermi level potential (E_F), the bent upward of the band gap of $BiVO_4$ and the bent downward of BiOBr will occur near the interface of compounds to reach equilibrium and create the built-in electric field in $BiOBr/BiVO_4$ (Figure 3c, middle). Under light illumination, the photogenerated electrons of BiOBr were driven by the built-in electric field to recombine with the photogenerated holes of $BiVO_4$ to achieve high charge separation/transfer efficiency.[31] Meanwhile, band bending also works as a one-way valve to inhibit the flow out of the charge carriers. Based on the results, $BiOBr/BiVO_4$ can efficiently separate the pollutant oxidation and CO_2 reduction to promote the activity of carbon source recovery.

3.2. Photocatalytic Pollutant Conversion Performance of the Catalysts. The carbon source recovery activity of the catalysts was assessed by the photocatalytic conversion of CBZ pollutants coupling the CO_2 reduction performed in a closed circulation system. Under solar spectrum irradiation, $BiOBr/BiVO_4$ with the ratio of 3:2 exhibited the best catalytic efficiency among the samples with different amounts of the compounds (Figure S10). As shown in Figures 4a and S11–S12, $BiOBr/BiVO_4$ can eliminate 86.12% of CBZ with nearly 10.23 $\mu mol \cdot g^{-1}$ CO selective production without H_2, O_2, or other liquid production in 4 h of light irradiation, which has a marked improvement compared to BiOBr, $BiVO_4$, and BiOBr +$BiVO_4$ (prepared via simple physical synthesis), illustrating the strong interaction between BiOBr and $BiVO_4$. In addition, the CO production over $BiOBr/BiVO_4$ hybrids strongly depends on the wavelength and absorption intensity (Figure 4b). The total organic carbon (TOC) measurement in Figure 4c shows the decrease of TOC along with the increase of inorganic carbon (IC), proving the efficient mineralization of CBZ to CO_2 which exists in the form of carbonate and bicarbonate. Afterward, the detection of the inorganic ions during the reaction in Figures 4d and S13 reveals the amount of CO_3^{2-} increases and then declines during the 4 h illumination, indicating the mineralization of organics and the dynamic accumulation−consumption−accumulation process with reaction time.[8,9] A similar change in the pH value during the one-pot conversion over $BiOBr/BiVO_4$ also exhibited the dynamic accumulation−consumption−accumulation process (Figure S14). In brief, $BiOBr/BiVO_4$ with directional charge transfer accomplished deep mineralization of organics instead of decomposition, meanwhile achieving an improvement in the subsequent CO_2 reduction to ingratiate the idea of a carbon-neutral economy.

The continuous and stable photocatalytic conversion of CBZ to CO with a negligible Bi^{3+} leaching concentration for four-run cycling and unchanged XRD spectra of $BiOBr/BiVO_4$ before and after the reaction suggested its stability and reusability, and $BiOBr/BiVO_4$ can efficiently convert CBZ as high as 40 ppm into CO, which was sufficient to meet the resource conversion in the actual wastewater (Figures S15–S17). Additionally, the appearance of new peaks positioned at 288.71 eV was attributed to the carbonate species in the $BiOBr/BiVO_4$ hybrids after the reaction (Figure S18), implying that the coupling of $BiVO_4$ and BiOBr conduced to the mineralization of CBZ rather than simple degradation. Afterward, we conducted quenching experiments by adding the scavengers to explain the active species in the systems. Since the catalytic experiment was carried out in a closed glass gas system without air, the quenching experiments were conducted by adding the isopropyl alcohol (IPA), triethanolamine (TEOA), *p*-benzoquinone (BQ), and dimethyl adipate (DMA) scavengers to capture the active species in the

https://doi.org/10.1021/acscatal.3c04820
ACS Catal. 2024, 14, 2134−2143

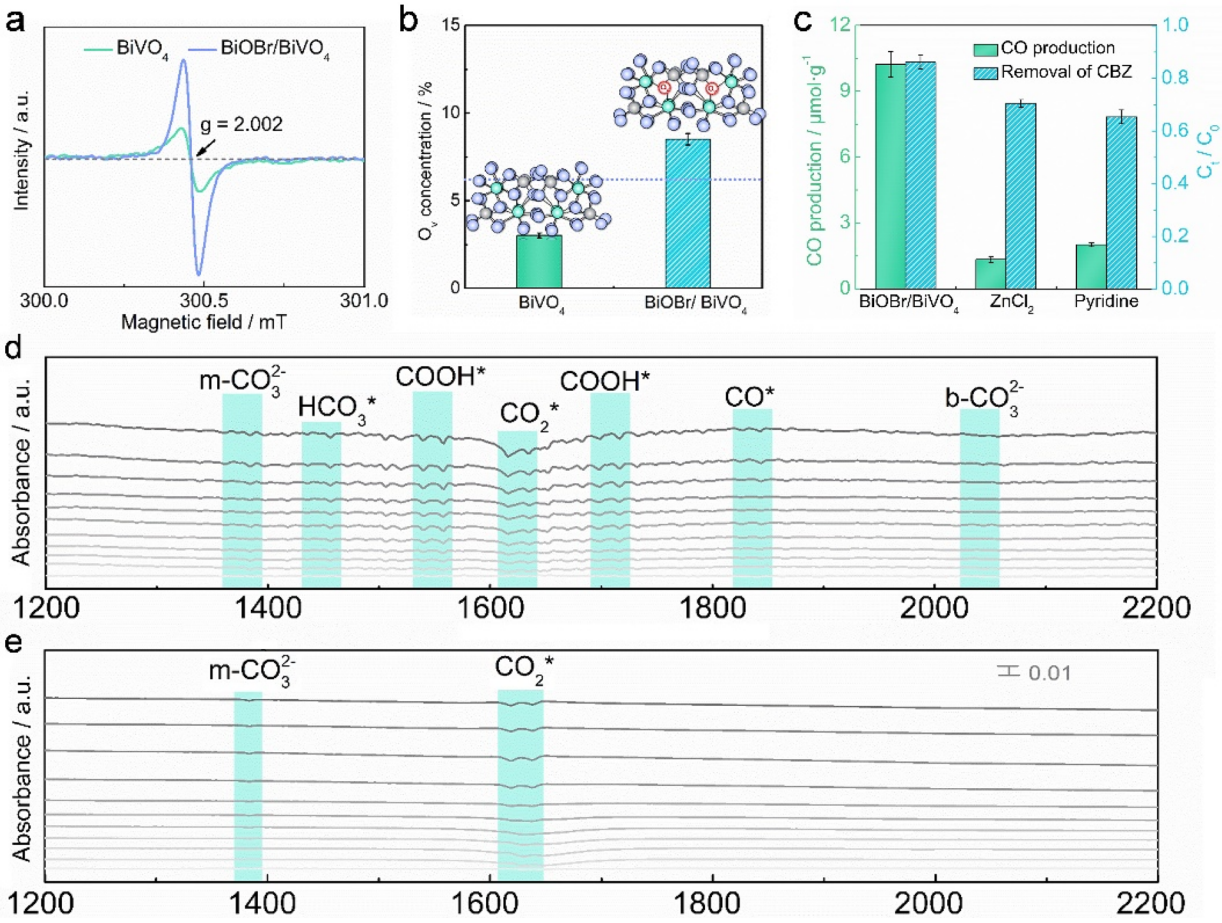

Figure 5. (a) EPR spectra and (b) quantitative experiment of the defects of $BiVO_4$ and $BiOBr/BiVO_4$. (c) Photocatalytic activity after addition of the LA or LB of $BiOBr/BiVO_4$. In situ DRIFTS spectra during the reaction were recorded over (d) $BiOBr/BiVO_4$ and (e) $BiOBr+BiVO_4$.

systems. As shown in Figures 4e and S19, the inhibitory effect of the scavengers illustrated h^+ played a key role followed by ·OH produced by its oxidation of water, while $\cdot O_2^-$ and $CO_3^{-}\cdot$ have no significant influence.[9,21] The observed EPR signal with characteristic peak intensity ratios of 1:2:2:1 in Figure 4f demonstrated the gradually increasing production of ·OH over time to mineralize CBZ and provide sufficient CO_2 for the subsequent recycling reaction.

3.3. Exploration of the Conversion Mechanism. To further explore the intrinsic atomic regulation and specific catalytic sites, the EPR spectra were measured to evaluate the spin electrons in the samples.[32] As shown in Figure 5a, the observed single Lorentz peak at $g = 2.002$ was ascribed to the free electrons trapped by the O_v.[33] The signal intensity of the O_v in $BiVO_4$ increased after coupling BiOBr, suggesting the increased content of the aqueous component of O_v. The surface O_v sites were further measured quantitatively by electron titration with thionine, the consumption of which corresponds to the content of electrons trapped in O_v sites.[34] As shown in Figures 5b and S20, the concentration of O_v sites of $BiVO_4$ and $BiOBr/BiVO_4$ evaluated from the consumption of thionine was 3.02% and 8.51%, respectively, while BiOBr had almost no oxygen vacancies. Generally, $BiVO_4$ theoretically has the intrinsic O_v which considerably originates from freeing oxygen of the $BiVO_4$ lattice, concomitantly leading to the delocalizing electrons around the VO_4^{3-} unit.[35] The concentrations of intrinsic O_v less than 6% did not alter the bandgap position of $BiVO_4$,[36] whereas the introduction of the $[Bi_2O_2]^+$ units in BiOBr markedly increased the content of O_v in $BiVO_4$, which gives rise to local structural distortions inside and induces the tendency to form small polarons at the surface to inhibit the charge recombination.[37] The efficient charge transmission of the catalyst that was in favor of the pollutant oxidation and CO_2 reduction separately occurs, while the key procedure of the one-pot conversion of the pollutant was the surface active sites in the catalysts to adsorb the produced CO_2 to ensure the synchronization of the oxidation and reduction reactions.[9] Therefore, we measured the molecular probe experiments in Figure 5c to trace the active sites in the catalysts. After the addition of $ZnCl_2$ or pyrrole (typical Lewis acid (LA) and Lewis base (LB)) in the reaction,[38,39] the CO production was greatly decreased while the CBZ removal had no significant change. To demonstrate the significance of the surface active sites in the catalysts, we measured the photocatalytic performance of $BiOBr/BiVO_4$ in the CO_2 atmosphere. As shown in Figure S21, the reduced CO production over $BiOBr/BiVO_4$ implies that the surface active sites in the catalysts can rapidly adsorb the generated CO_2 molecule from CBZ, which also suppresses the surface HER (hydrogen evolution reaction). It can be speculated that LA and LB can block the surface active sites to prohibit CO_2 adsorption and activation. Therefore, the results concluded that the O_v (LA) and its proximal surface hydroxyls (LB) will form defect-induced frustrated Lewis acid−base pairs (DFLPs) as active sites to provide a unique route to adsorb and activate CO_2.

https://doi.org/10.1021/acscatal.3c04820
ACS Catal. 2024, 14, 2134−2143

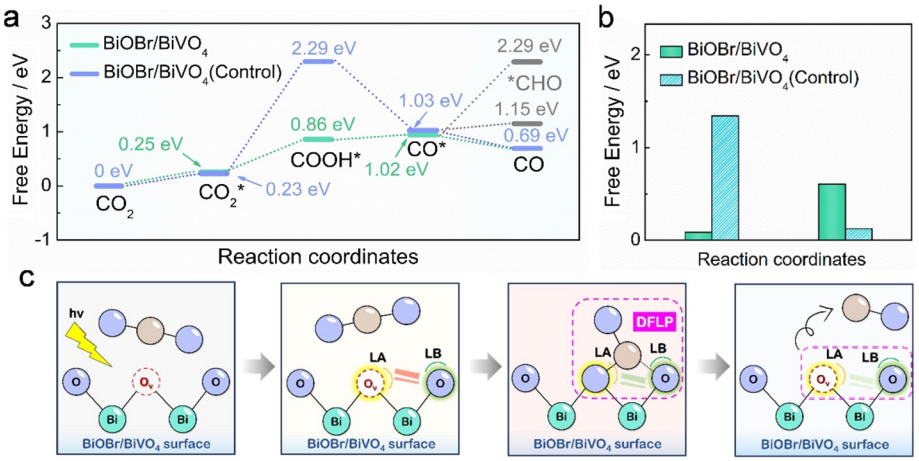

Figure 6. (a) Calculated free energy diagram for the CO_2−CO conversion and (b) calculated reaction free energy of COOH* (left) and CHO* (right) based on the same initial state of CO_2* production on $BiOBr/BiVO_4$ and $BiOBr/BiVO_4$ (Control). (c) Schematic illustration of the CO_2 conversion over the artificial surface active site of $BiOBr/BiVO_4$.

In situ diffuse reflection Fourier transform infrared spectroscopy (DRIFTS) analyses were carried out to investigate the intermediates during the reaction. As shown in Figure 5d, the new peaks at 1618 and 1633 cm^{-1} (assigned to the adsorbed CO_2*) appeared and gradually increased with the irradiation time prolonged, indicating the efficient adsorption and activation of CO_2 over $BiOBr/BiVO_4$.[40,41] Subsequently, an incremental peak around 1530−1560 cm^{-1} and 1690−1720 cm^{-1} appeared, suggesting the formation and accumulation of COOH*. The peaks at 1840 and 1824 cm^{-1}, which correspond to CO*, illustrate the dehydroxylation of COOH* and the final product of CO, and the formed bicarbonate (HCO_3*, 1436 and 1456 cm^{-1}), monodentate carbonate (m-CO_3^{-2}, 1361 and 1382 cm^{-1}), and bidentate carbonate (b-CO_3^{2-}, 2044 cm^{-1}) demonstrate the reduced CO_2 was from the mineralization of CBZ. Oppositely, only a few m-CO_3^{2-} and CO_2* can be detected over the $BiOBr+BiVO_4$ sample in Figure 5e, verifying the strong internal interaction between $BiOBr/BiVO_4$ to boost the photocatalytic carbon source recovery from pollutants. Based on the results, the possible pathway to recycle the carbon source from CBZ over $BiOBr/BiVO_4$ may proceed as follows: (1) the adsorption of the generated CO_2 from CBZ; (2) the activation of adsorbed CO_2* to give a carboxyl COOH*; (3) the reduction and subsequent dissociation of COOH* to produce CO* via a proton−electron transfer reduction process; and (4) the desorption of CO.

3.4. Possible One-Pot Pollutant Conversion Mechanism of the Catalysts. The free energy of five successive reaction steps including CO_2 adsorption, proton-coupled electron transfer to form the COOH* intermediate, dehydroxylation to produce CO*, hydrogenation of CO*, and CO desorption on the catalysts was calculated to explore the mechanism of CO_2 conversion in Figure 6a. The formation of COOH* was an endergonic reaction with high energy input which was the rate-limiting step in the CO_2−CO process.[42] Less reaction energy (0.86 eV) was required for $BiOBr/BiVO_4$ than $BiOBr/BiVO_4$ (Control) (a simple heterojunction with fewer O_v, 2.29 eV) to realize the transformation of CO_2* to COOH*. The restraint of the hydrogenation of CO* was a critical step to selectively produce CO. Compared with $BiOBr/BiVO_4$ (Control) having continuously energy-favorable hydrogenation (0.12 eV), the barrier to form CHO* exhibited 1.34 eV at $BiOBr/BiVO_4$ (Figure 6b), causing the preferential energy-favorable desorption from the CO* intermediate to CO instead of further hydrogenation. These results suggested the oxygen defect induced the oriented charge transfer and surface active sites on $BiOBr/BiVO_4$ to reduce the energy barrier of the key rate-limiting step to convert CBZ to CO with high selectivity.

To detect the intermediates of the mineralization pathway of CBZ, we performed UHPLC-MS analysis under the optimum conditions. Based on the results and previous studies of the ten identified products, we propose three different degradation pathways to eliminate CBZ in Figures S25−S26 including the hydroxylation, attack of the C=C, and the oxidation of the −OH group.[43] Hence, the mechanism of the carbon recovery part during the conversion of pollutants over $BiOBr/BiVO_4$ was proposed in Figure 6c. Due to the large steric hindrance between LA and LB, the constructed DFLP on $BiVO_4$ will create an active region to efficiently and rapidly capture CO_2 mineralized from CBZ. Subsequently, the occupied π orbitals of CO_2 will donate their electrons to empty d orbitals of the LA centers, and the empty σ^* orbitals of CO_2 accept the electrons from the electron-rich LB sites to form the unique CO_2 adsorption mode.[44,45] Benefiting from the orbital interaction between the bonding and antibonding orbitals of the molecule, absorbed CO_2 can be synergetically activated. Finally, the CO* intermediate will be desorbed to CO, and the O* will be reduced to H_2O by one more photogenerated electron, restoring the catalyst to its original state.

4. CONCLUSION

In conclusion, we developed the $BiOBr/BiVO_4$ photocatalyst enriched with surface oxygen defects that induced the synergetic effect to convert the CBZ pollutant into CO with high selectivity (~100%) to ingratiate carbon neutrality. The synergetic effect includes constructed directional charge transfer from BiOBr to $BiVO_4$ to produce the active radical to photodegradation of CBZ into CO_2, coupling the established active DFLP sites to efficiently absorb and activate CO_2. Furthermore, the surface DFLP in the $BiOBr/BiVO_4$ decreased the energy barrier to produce COOH* and inhibited the hydrogenation of CO*, realizing the high selective generation of CO. This system suggested a feasible strategy to achieve the goal of carbon neutrality to sustainably convert

https://doi.org/10.1021/acscatal.3c04820
ACS Catal. 2024, 14, 2134−2143

the organic pollutants into value-added chemical feedstocks and offered worthy guidance for realizing carbon source recovery in practical wastewater treatment.

■ ASSOCIATED CONTENT

Supporting Information

The Supporting Information is available free of charge at https://pubs.acs.org/doi/10.1021/acscatal.3c04820.

Synthesis process, characterization technique, and computational method details; raw data of catalytic performance evaluation, ion chromatography, and UPLC-MS spectra; characterization data such as SEM, HRTEM, and SAED images and EDX elemental mappings, steady-state PL spectra, and electrochemical characterization; XPS spectra; XRD patterns; construction of models; schematic illustration of the possible catalytic mechanism; table of the fluorescence lifetime of the different components and comparison of the photocatalytic performance in this paper with that of a recently reported similar reaction system (PDF)

■ AUTHOR INFORMATION

Corresponding Author

Jian-Ping Zou − *Key Laboratory of Jiangxi Province for Persistent Pollutants Control and Resources Recycle, Nanchang Hangkong University, Nanchang 330063, P. R. China; Key Laboratory of Poyang Lake Environment and Resource Utilization of Ministry of Education, School of Resources Environmental and Chemical Engineering, Nanchang University, Nanchang 330031, P. R. China;* orcid.org/0000-0002-3585-6541; Email: zjp_112@126.com

Authors

Ling-Ling Zheng − *Key Laboratory of Jiangxi Province for Persistent Pollutants Control and Resources Recycle, Nanchang Hangkong University, Nanchang 330063, P. R. China; Key Laboratory of Poyang Lake Environment and Resource Utilization of Ministry of Education, School of Resources Environmental and Chemical Engineering, Nanchang University, Nanchang 330031, P. R. China*

Lei Tian − *Key Laboratory of Jiangxi Province for Persistent Pollutants Control and Resources Recycle, Nanchang Hangkong University, Nanchang 330063, P. R. China; Key Laboratory of Poyang Lake Environment and Resource Utilization of Ministry of Education, School of Resources Environmental and Chemical Engineering, Nanchang University, Nanchang 330031, P. R. China*

Long-Shuai Zhang − *Key Laboratory of Jiangxi Province for Persistent Pollutants Control and Resources Recycle, Nanchang Hangkong University, Nanchang 330063, P. R. China*

Jian Yu − *Key Laboratory of Jiangxi Province for Persistent Pollutants Control and Resources Recycle, Nanchang Hangkong University, Nanchang 330063, P. R. China*

Ying Chen − *Key Laboratory of Jiangxi Province for Persistent Pollutants Control and Resources Recycle, Nanchang Hangkong University, Nanchang 330063, P. R. China; Key Laboratory of Poyang Lake Environment and Resource Utilization of Ministry of Education, School of Resources Environmental and Chemical Engineering, Nanchang University, Nanchang 330031, P. R. China*

Qian Fu − *Key Laboratory of Jiangxi Province for Persistent Pollutants Control and Resources Recycle, Nanchang Hangkong University, Nanchang 330063, P. R. China; Key Laboratory of Poyang Lake Environment and Resource Utilization of Ministry of Education, School of Resources Environmental and Chemical Engineering, Nanchang University, Nanchang 330031, P. R. China*

Xiao-Zhen Liu − *Key Laboratory of Poyang Lake Environment and Resource Utilization of Ministry of Education, School of Resources Environmental and Chemical Engineering, Nanchang University, Nanchang 330031, P. R. China*

Dai-She Wu − *Key Laboratory of Poyang Lake Environment and Resource Utilization of Ministry of Education, School of Resources Environmental and Chemical Engineering, Nanchang University, Nanchang 330031, P. R. China*

Complete contact information is available at: https://pubs.acs.org/10.1021/acscatal.3c04820

Notes

The authors declare no competing financial interest.

■ ACKNOWLEDGMENTS

We gratefully acknowledge the financial support of the National Natural Science Foundation of China (51938007, 52170082, 52100186, and 52260006) and the Jiangxi Provincial Natural Science Foundation (20212ACB203008 and 20225BCJ23003).

■ REFERENCES

(1) Liras, M.; Barawi, M.; O'Shea, V. Hybrid materials based on conjugated polymers and inorganic semiconductors as photocatalysts: from environmental to energy applications. *Chem. Soc. Rev.* **2019**, *48*, 5454−5487.

(2) Tian, L.; Zhang, L. S.; Zheng, L. L.; Chen, Y.; Din, L.; Fan, J. P.; Wu, D. S.; Zou, J. P.; Luo, S. L. Overcoming Electrostatic Interaction via Strong Complexation for Highly Selective Reduction of CN^- into N_2. *Angew. Chem., Int. Ed.* **2022**, *61*, e202214145.

(3) Zhao, K.; Quan, X.; Su, Y.; Qin, X.; Chen, S.; Yu, H. T. Enhanced chlorinated pollutant degradation by the synergistic effect between dechlorination and hydroxyl radical oxidation on a bimetallic single-atom catalyst. *Environ. Sci. Technol.* **2021**, *55*, 14194−14203.

(4) Xu, S. Z.; Carter, E. A. Theoretical Insights into Heterogeneous (Photo)electrochemical CO_2 Reduction. *Chem. Rev.* **2019**, *119*, 6631−6669.

(5) Zheng, L. L.; Zhang, J.; Liu, X. Z.; Tian, L.; Xiong, Z. S.; Xiong, X.; Chen, P.; Wu, D. S.; Zou, J. P. Degradation of pesticide wastewater with simultaneous resource recovery via ozonation coupled with anaerobic biochemical technology. *Chemosphere* **2022**, *300*, 134520.

(6) Sun, K.; Qian, Y. Y.; Jiang, H. L. Metal-Organic Frameworks for Photocatalytic Water Splitting and CO_2 Reduction. *Angew. Chem., Int. Ed.* **2023**, *62*, e202217565.

(7) Tang, B.; Xiao, F. X. An Overview of Solar-Driven Photoelectrochemical CO_2 Conversion to Chemical Fuels. *ACS Catal.* **2022**, *12*, 9023−9057.

(8) Ran, M. X.; Xu, H.; Bao, Y.; Zhang, Y. Y.; Zhang, J. L.; Xing, M. Y. Selective production of CO from organic pollutants by coupling piezocatalysis and advanced oxidation processes. *Angew. Chem., Int. Ed.* **2023**, *135*, e202303728.

(9) Zou, J. P.; Wu, D. D.; Luo, J. M.; Xing, Q. J.; Luo, X. B.; Dong, W. H.; Luo, S. L.; Du, H. M.; Sui, S. L. A Strategy for One-Pot Conversion of Organic Pollutants into Useful Hydrocarbons through Coupling Photodegradation of MB with Photoreduction of CO_2. *ACS Catal.* **2016**, *6*, 6861−6867.

(10) Liu, W. Y.; Fu, P. B.; Zhang, Y. Y.; Xu, H.; Wang, H. L.; Xing, M. Y. Efficient hydrogen production from wastewater remediation by piezoelectricity coupling advanced oxidation processes. *Proc. Natl. Acad. Sci. U.S.A.* **2023**, *120*, e2218813120.
(11) Zou, J. P.; Chen, Y.; Liu, S. S.; Xing, Q. J.; Dong, W. H.; Luo, X. B.; Dai, W. L.; X, X.; Luo, J. M.; Crittenden, J. Electrochemical oxidation and advanced oxidation processes using a 3D hexagonal Co_3O_4 array anode for 4-nitrophenol decomposition coupled with simultaneous CO_2 conversion to liquid fuels via a flower-like CuO cathode. *Water Res.* **2019**, *150*, 330−339.
(12) Zhang, L. S.; Jiang, X. H.; Zhong, Z. A.; Tian, L.; Sun, Q.; Cui, Y. T.; Lu, X.; Zou, J. P.; Luo, S. L. Carbon nitride supported high loading Fe single-atom catalyst for activation of peroxymonosulfate to generate $^1O_2$ with 100% selectivity. *Angew. Chem., Int. Ed.* **2021**, *60*, 21751−21755.
(13) Lu, L.; Guest, J. S.; Peters, C. A.; Zhu, X. P.; Rau, G. H.; Ren, Z. Y. Wastewater treatment for carbon capture and utilization. *Nat. Sustain.* **2018**, *1*, 750−758.
(14) Zhang, L. L.; Wang, Y. B. Decoupled Artificial Photosynthesis. *Angew. Chem., Int. Ed.* **2023**, *62*, e202219076.
(15) Lin, W.; Lin, J.; Zhang, X.; Zhang, L. L.; Borse, R. A.; Wang, Y. B. Decoupled Artificial Photosynthesis via a Catalysis-Redox Coupled COF||$BiVO_4$ Photoelectrochemical Device. *J. Am. Chem. Soc.* **2023**, *145*, 18141−18147.
(16) Liu, Q.; Wang, S. H.; Mo, W. H.; Zheng, Y. Y.; Xu, Y. B.; Yang, G. D.; Zhong, S. X.; Ma, J.; Liu, D.; Bai, S. Emerging stacked photocatalyst design enables spatially separated $Ni(OH)_2$ redox cocatalysts for overall CO_2 reduction and H_2O oxidation. *Small* **2022**, *18*, 2104681.
(17) Barlow, J. M.; Ziller, J. W.; Yang, J. Y. Inhibiting the hydrogen evolution reaction (HER) with proximal cations: a strategy for promoting selective electrocatalytic reduction. *ACS Catal.* **2021**, *11*, 8155−8164.
(18) Dai, W. L.; Wang, P.; Long, J. F.; Xu, Y.; Zhang, M.; Yang, L. X.; Zou, J. P.; Luo, X. B.; Luo, S. L. Constructing Robust Bi Active Sites In Situ on α-Bi_2O_3 for Efficient and Selective Photoreduction of CO_2 to CH_4 via Directional Transfer of Electrons. *ACS Catal.* **2023**, *13*, 2513−2522.
(19) Wang, Y. C.; Ren, B. Y.; Ou, J. Z.; Xu, K.; Yang, C. H.; Li, Y. X.; Zhang, H. J. Engineering two-dimensional metal oxides and chalcogenides for enhanced electro- and photocatalysis. *Sci. Bull.* **2021**, *66*, 1228−1252.
(20) Shi, M.; Li, G. N.; Li, J. M.; Jin, X.; Tao, X. P.; Zeng, B.; Pidko, E. A.; Li, R. G.; Li, C. Intrinsic facet-dependent reactivity of well-defined BiOBr nanosheets on photocatalytic water splitting. *Angew. Chem., Int. Ed.* **2020**, *132*, 6652−6657.
(21) Zheng, L. L.; Tian, L.; Wang, D. K.; Chen, Y.; Tang, Q. Q.; Xing, Q. J.; Liu, X. Z.; Wu, D. S.; Zou, J. P. Facet engineering of $BiVO_4$ photocatalyst for the synergetic adsorption and activation of persulfate for organic pollutants degradation. *Chem. Eng. J.* **2023**, *473*, 145507.
(22) Li, R. G.; Zhang, F. X.; Wang, D. G.; Yang, J. X.; Li, M. R.; Zhu, J.; Zhou, X.; Han, H. X.; Li, C. Spatial separation of photogenerated electrons and holes among {010} and {110} crystal facets of $BiVO_4$. *Nat. Commun.* **2013**, *4*, 1432.
(23) Lin, S.; Huang, H. W.; Ma, T. Y.; Zhang, Y. H. Photocatalytic oxygen evolution from water splitting. *Adv. Sci.* **2021**, *8*, 2002458.
(24) Fareza, A. R.; Nugroho, F. A. A.; Abdi, F. F.; Fauzia, V. Nanoscale metal oxides-2D materials heterostructures for photo-electrochemical water splitting-a review. *J. Mater. Chem. A* **2022**, *10*, 8656−8686.
(25) Li, M.; Yu, S. X.; Huang, H. W.; Li, X. W.; Feng, Y. B.; Wang, C.; Wang, Y. G.; Ma, T. Y.; Guo, L.; Zhang, Y. H. Unprecedented Eighteen-Faceted BiOCl with a Ternary Facet Junction Boosting Cascade Charge Flow and Photo-redox. *Angew. Chem., Int. Ed.* **2019**, *58*, 9517−9521.
(26) Chu, C. H.; Zhu, Q. H.; Pan, Z. H.; Gupt, S.; Huang, D. H.; Du, Y. H.; Weon, S. H.; Wu, Y. S.; Muhich, C.; Stavitski, E.; Domen, K.; Kim, J. H. Spatially separating redox centers on 2D carbon nitride with cobalt single atom for photocatalytic H_2O_2 production. *PNAS.* **2020**, *117*, 6376−6382.
(27) Li, Y. K.; Wang, L.; Zhang, F.; Zhang, W. T.; Shao, G. S.; Zhang, P. Detecting and Quantifying Wavelength Dependent Electrons Transfer in Heterostructure Catalyst via In Situ Irradiation XPS. *Adv. Sci.* **2023**, *10*, 2205020.
(28) Wang, L.; Li, Y. K.; Wu, C.; Li, X.; Shao, G. S.; Zhang, P. Tracking charge transfer pathways in $SrTiO_3$/CoP/Mo_2C nanofibers for enhanced photocatalytic solar fuel production. *Chin. J. Catal.* **2022**, *43*, 507−518.
(29) Chen, D.; Lu, R. H.; Yu, R. H.; Dai, Y. H.; Zhao, H. Y.; Wu, D. L.; Wang, P. Y.; Zhu, J. W.; Pu, Z. H.; Chen, L.; Yu, J.; Mu, S. C. Work-function-induced interfacial built-in electric fields in O_S-O_SSe_2 heterostructures for active acidic and alkaline hydrogen evolution. *Angew. Chem., Int. Ed.* **2022**, *61*, e202208642.
(30) Chen, Y.; Mu, Y.; Tian, L.; Zheng, L. L.; Xing, Y.; Mei, Q. J.; Liu, W.; Zou, J. P.; Yang, L. X.; Luo, S. L.; Wu, D. S. Targeted Decomplexation of Metal Complexes for Efficient Metal Recovery by Ozone/Percarbonate. *Environ. Sci. Technol.* **2023**, *57*, 5034−5045.
(31) Xia, B. Q.; He, B. W.; Zhang, J. J.; Li, L. Q.; Zhang, Y. Z.; Yu, J. G.; Ran, J. R.; Qiao, S. Z. TiO_2/$FePS_3$ S-Scheme Heterojunction for Greatly Raised Photocatalytic Hydrogen Evolution. *Adv. Energy Mater.* **2022**, *12*, 2201449.
(32) Ye, F. H.; Zhang, S. S.; Cheng, Q. Q.; Long, Y. D.; Liu, D.; Paul, R.; Fang, Y. M.; Su, Y. Q.; Qu, L. T.; Dai, L. M.; Hu, C. G. The role of oxygen-vacancy in bifunctional indium oxyhydroxide catalysts for electrochemical coupling of biomass valorization with CO_2 conversion. *Nat. Commun.* **2023**, *14*, 2040.
(33) Liu, S. D.; Wang, H. Y.; Wang, S.; Dai, Y. L.; Liu, B.; Liu, Y.; Dang, F. X.; Smith, K.; Nie, X. W.; Hou, S. D.; Guo, X. W. Engineering Morphology and Ni Substitution of $NixCo_{3-x}O_4$ Spinel Oxides to Promote Catalytic Combustion of Ethane: Elucidating the Influence of Oxygen Defects. *ACS Catal.* **2023**, *13*, 4683−4699.
(34) Wu, X. J.; Li, J. Q.; Xie, S. J.; Duan, P. B.; Zhang, H. K.; Feng, J.; Zhang, Q. H.; Cheng, J.; Wang, Y. Selectivity Control in Photocatalytic Valorization of Biomass-Derived Platform Compounds by Surface Engineering of Titanium Oxide. *Chem.* **2020**, *6*, 3038−3053.
(35) Wang, W. N.; Strohbeen, P. J.; Lee, D. H.; Zhou, C. Y.; Kawasaki, J. K.; Choi, K. S.; Liu, M. Z.; Galli, G. L. The Role of Surface Oxygen Vacancies in $BiVO_4$. *Chem. Mater.* **2020**, *32*, 2899−2909.
(36) Lee, D. H.; Wang, W.; Zhou, C. Y.; Tong, X.; Liu, M. Z.; Galli, G.; Choi, K. S. The impact of surface composition on the interfacial energetics and photoelectrochemical properties of $BiVO_4$. *Nat. Energy* **2021**, *6*, 287−294.
(37) Wang, W.; Favaro, M.; Chen, E.; Trotochaud, L.; Bluhm, H.; Choi, K. S.; Krol, R.; Starr, E. D.; Galli, G. Influence of Excess Charge on Water Adsorption on the $BiVO_4$(010) Surface. *J. Am. Chem. Soc.* **2022**, *144*, 17173−17185.
(38) Yan, T. J.; Li, L. N.; Wang, L.; Ran, W. G.; Duchesne, P. N.; Wan, L. L.; Nguyen, N. T.; Wang, L.; Xia, M. K.; Ozin, G. A. Bismuth atom tailoring of indium oxide surface frustrated Lewis pairs boosts heterogeneous CO_2 photocatalytic hydrogenation. *Nat. Commun.* **2020**, *11*, 6095.
(39) Sheng, J. P.; He, Y. M.; Huang; Yuan, C. W.; Wang, S. Y.; Dong, F. Frustrated lewis pair sites boosting CO_2 photoreduction on Cs_2CuBr_4 perovskite quantum dots. *ACS Catal.* **2022**, *12*, 2915−2926.
(40) Li, J.; Huang, H. L.; Xue, W. J.; Sun, K.; Song, X. H.; Wu, C. R.; Nie, L.; Li, Y.; Liu, C. Y.; Pan, Y.; Jiang, H. L.; Mei, D. H.; Zhong, C. L. *Nat. Catal.* **2021**, *4*, 719−729.
(41) Liu, Q.; Cheng, H.; Chen, T. X.; Benedict, T. W.; Xiang, Z. M.; Wang, F. X. Regulating the *OCCHO intermediate pathway towards highly selective photocatalytic CO_2 reduction to CH_3CHO over locally crystallized carbon nitride. *Energy Environ. Sci.* **2022**, *15*, 225−233.
(42) van der Zee, L. J. C.; Pahar, S.; Richards, E.; Melen, R. L.; Slootweg, J. C. Insights into single-electron-transfer processes in

https://doi.org/10.1021/acscatal.3c04820
ACS Catal. 2024, 14, 2134−2143

frustrated Lewis pair chemistry and related donor-acceptor systems in main group chemistry. *Chem. Rev.* **2023**, *123*, 9653−9675.
(43) Yang, Y. H.; Ramos, N. C.; Clark, J.; Hillhouse, H. Electrochemical oxidation of pharmaceuticals in synthetic fresh human urine: Using selective radical quenchers to reveal the dominant degradation pathways and the scavenging effects of individual urine constituents. *Water Res.* **2022**, *221*, 118722.
(44) Chen, H.; Xiong, C. Y.; Moon, J. S.; Ivanov, A. S.; Lin, W. W.; Wang, T.; Fu, J.; Jiang, D. E.; Wu, Z. L.; Yang, Z. Z.; Dai, S. Defect-regulated frustrated-lewis-pair behavior of boron nitride in ambient pressure hydrogen activation. *J. Am. Chem. Soc.* **2022**, *144*, 10688−10693.
(45) Yin, J.; Jin, J.; Yin, Z. Y.; Zhu, L.; Du, X.; Peng, Y.; Xi, P. X.; Yan, C. H.; Sun, S. H. The built-in electric field across FeN/Fe_3N interface for efficient electrochemical reduction of CO_2 to CO. *Nat. Commun.* **2023**, *14*, 1724.

https://doi.org/10.1021/acscatal.3c04820
ACS Catal. 2024, 14, 2134−2143